

See discussions, stats, and author profiles for this publication at: <https://www.researchgate.net/publication/228903074>

Computational Study of Flow Regimes in Vertical Pneumatic Conveying

ARTICLE *in* INDUSTRIAL & ENGINEERING CHEMISTRY RESEARCH · JULY 2009

Impact Factor: 2.59 · DOI: 10.1021/ie900230s

CITATIONS

23

READS

127

3 AUTHORS, INCLUDING:



Shibo Kuang

Monash University (Australia)

29 PUBLICATIONS 273 CITATIONS

SEE PROFILE



Aibing Yu

University of New South Wales

622 PUBLICATIONS 11,725 CITATIONS

SEE PROFILE

Computational Study of Flow Regimes in Vertical Pneumatic Conveying

S. B. Kuang,[†] A. B. Yu,^{*,†} and Z. S. Zou[‡]

Lab for Simulation and Modelling of Particulate Systems, School of Materials Science and Engineering, The University of New South Wales, Sydney, NSW 2052, Australia, and School of Materials Science and Metallurgy, Northeastern University, Shenyang, Liaoning 110004, P. R. China

Pneumatic conveying is an important technology in industries to transport bulk materials from one location to another. Different flow regimes have been observed in such a transportation process depending on operational conditions, but the underlying fundamentals are not clear. This paper presents a three-dimensional numerical study of vertical pneumatic conveying by a combined approach of discrete element model for particles and computational fluid dynamics for gas. The approach is verified by comparing the calculated and measured results in terms of particle flow pattern and gas pressure drop. It is shown that flow regimes usually encountered in vertical pneumatic conveying and their corresponding phase diagram can be reproduced. Then forces governing the behavior of particles, such as the particle–particle, particle–fluid, and particle–wall forces, are analyzed in detail. It is shown that the roles of these forces vary with flow regimes. A new phase diagram is proposed in terms of the key forces, which can successfully identify dilute-phase flow and dense-phase flow in vertical pneumatic conveying.

1. Introduction

Pneumatic conveying is one of the most commonly used methods of transporting granular materials in industry. Depending on materials to be handled, operational condition, and system geometry, such transportation can take place in different flow regimes including slug flow and dispersed flow. A suitable flow regime can minimize power consumption, solid breakage, and pipe abrasion and avoid flow blockage during transportation.^{1,2} Therefore, it has been widely studied over the past decades, mainly on the basis of experimental measurements.^{2–14} These studies are useful, particularly in solving some practical problems. However, to date, the mechanisms underlying the flow regimes identified and their transition are not clearly understood. This has hindered the development of a general method for reliable scale-up, design, control, and optimization of pneumatic conveying.

Flow regime as a bulk behavior is the result of the collective interactions between particles, particle and wall, and particle and fluid. Analysis of the interaction forces can help understand the underlying mechanisms. However, at this stage of development it is not possible to experimentally generate such detailed force information, especially for particle–particle and particle–fluid forces. In principle, numerical methods can overcome this difficulty, which may be continuum- or discrete-based with respect to the solid phase. The former is typically represented by the so-called two-fluid model (TFM).^{15–20} TFM is computationally convenient, but its effective use heavily depends on the constitutive or closure relations which are not generally available for the solid phase at this stage of development. The discrete approach can be done by means of the Lagrangian particle tracking (LPT) method^{21,22} or the combined approach of computational fluid dynamics (CFD) for gas phase and discrete element model (DEM) for solid phase.^{23,24} LPT is valid for gas–solid flow where the solid concentration is low and hence particle–particle interaction is not important. On the

contrary, CFD–DEM has no such a limit and is thus applicable to a wide range of flow conditions.^{25–28}

With this realization, in recent years, CFD–DEM has been increasingly used to study pneumatic conveying in various aspects, including slug flow as summarized by Kuang et al.,²⁹ heat transfer,³⁰ attrition,^{31,32} and electrification,^{33–35} phenomena in bends,^{36,37} and flow regimes.^{38,39} These studies have improved our understanding of pneumatic conveying. However, most of them were based on some simplified models where three-dimensional (3D) particle flow was sometimes treated as 2D and gas flow was 2D or 1D. Because of this, some key flow features in pneumatic conveying are missing in the previous studies. For example, using 2D CFD–DEM, Lim et al.³⁸ obtained slug flow and dispersed flow in horizontal and vertical pipes; however, the stratified flow and the settled layers of slug flow in the horizontal pipe and the falling particles at the back of a slug in the vertical pipe were not numerically reproduced as observed in the experiments.^{8,40–43} Fraige and Langston³⁹ predicted three typical flow regimes, that is, slug flow, stratified flow, and dispersed flow in horizontal pneumatic conveying by a 1D CFD–3D DEM model. However, in their work, particle rotation in DEM was arbitrarily assumed corresponding to different flow regimes. In addition, in the above two studies, short pipes ($L/D \leq 25$) have been considered using periodic boundary condition (PBC). Although computationally efficient, PBC-based CFD–DEM models proposed thus far do not fix solid flow rate at varying gas velocities. Therefore, they cannot be used to predict the well-recognized phase diagram which is a plot of pressure drop versus gas velocity for constant solid flow rates and proved to be useful for understanding the transition of flow regimes. This problem does not exist in the study of vertical slug flow conducted by Strauß et al.,⁴⁰ where a relatively long pipe ($L/D = 75$) has been simulated by a 3D CFD–DEM model without PBC. However, in the so-called 3D model, the gas flow was simply described by the Darcy law to avoid CFD effort, hereby an incomplete phase diagram only with the dense-phase flow was produced. Therefore, to date, there is no publication reporting a successful prediction of the phase diagram as observed in physical experiments on the basis of CFD–DEM simulations. Moreover, the previous CFD–DEM

* To whom correspondence should be addressed. Tel: +61 2 93854429. Fax: +61 2 93855856. E-mail: a.yu@unsw.edu.au.

[†] The University of New South Wales.

[‡] Northeastern University.

studies of flow regimes mainly focus on the production of solid patterns, with no efforts made to analyze particle–particle, particle–wall and particle–fluid forces that are directly related to the underlying mechanisms.

This paper presents a numerical study of the flow regimes in a long vertical pipe ($L/D = 125$) by means of a 3D CFD–DEM approach to overcome the problems with the previous studies. The validity of the approach is examined by comparing the numerical and experimental results in terms of particle flow patterns and gas pressure drop. On the basis of the simulated results, the interaction forces between particles, particle and fluid, and particle and wall are analyzed in detail. The results show that the different flow regimes result from the variation of the relative importance of these forces.

2. Simulation Method

The current 3D CFD–DEM model is in principle the same as our previous 2D CFD–3D DEM model in the study of horizontal slug flow.²⁹ For completeness, below we only describe the key features of the model.

2.1. Governing Equations for Particle Flow. The solid phase is treated as a discrete phase that is described by DEM. Hence, the translational and rotational motions of a particle are determined by Newton's second law of motion, that is,

$$m_i \frac{d\mathbf{v}_i}{dt} = \mathbf{f}_{pgf,i} + \mathbf{f}_{drag,i} + \sum_{j=1}^{k_i} (\mathbf{f}_{c,ij} + \mathbf{f}_{d,ij}) + m_i \mathbf{g} \quad (1)$$

and

$$I_i \frac{d\boldsymbol{\omega}_i}{dt} = \sum_{j=1}^{k_i} (\mathbf{T}_{t,ij} + \mathbf{T}_{r,ij}) \quad (2)$$

where m_i , I_i , \mathbf{v}_i , and $\boldsymbol{\omega}_i$ are, respectively, the mass, momentum of rotational inertia, translational and rotational velocities of particle i . The forces involved are (1) the pressure gradient force, given by $\mathbf{f}_{pgf,i} = -\nabla P V_i$, where P and V_i are the fluid pressure and the volume of particle i , respectively; (2) the fluid drag force, calculated by $\mathbf{f}_{drag,i} = \mathbf{f}_{drag0,i} \varepsilon_{f,i}^{-\chi}$,⁴⁴ where $\mathbf{f}_{drag0,i}$, χ and $\varepsilon_{f,i}$ are, respectively, the fluid drag force on particle i in the absence of other particles, the equation coefficient, and the local porosity for the particle; (3) the gravity force, $m_i \mathbf{g}$; and (4) the interparticle forces between particles i and j , which include the elastic contact force, $\mathbf{f}_{c,ij}$, and the viscous contact damping force, $\mathbf{f}_{d,ij}$. The torque acting on particle i by particle j includes two components. One arises from the tangential forces, given by $\mathbf{T}_{t,ij} = \mathbf{R}_{i,j} \times (\mathbf{f}_{ct,ij} + \mathbf{f}_{dt,ij})$, where $\mathbf{R}_{i,j}$ is a vector from the mass center to the contact point; and the another one is the rolling friction torque given by $\mathbf{T}_{r,ij} = \mu_{r,ij} d_i |\mathbf{f}_{n,ij}| \hat{\boldsymbol{\omega}}_i$,⁴⁵ where $\mu_{r,ij}$ and d_i are rolling coefficient and particle diameter, respectively. The second torque is attributed to the elastic hysteresis loss and viscous dissipation in relation to particle–particle or particle–wall contact, and slows down the relative rotations of particles. For a particle undergoing multiple interactions, the individual interaction forces and torques are summed over the k_i particles in contact with particle i . The interparticle or particle–wall force is calculated according to the nonlinear models commonly used in DEM.²⁵ The equations to calculate these forces are the same as those employed in our previous studies.^{29,45–47}

2.2. Governing Equations for Gas Flow. The gas flow is treated as a continuous phase and modeled in a way similar to the one in the conventional two-fluid modeling. Thus, its governing equations are the conservation of mass and momen-

tum in terms of local mean variables over a computational cell, given by

$$\frac{\partial(\rho_f \varepsilon_f)}{\partial t} + \nabla \cdot (\rho_f \varepsilon_f \mathbf{u}) = 0 \quad (3)$$

and

$$\frac{\partial(\rho_f \varepsilon_f \mathbf{u})}{\partial t} + \nabla \cdot (\rho_f \varepsilon_f \mathbf{u} \mathbf{u}) = -\nabla P - \frac{\sum_{i=1}^{k_c} (\mathbf{f}_{drag,i} + \mathbf{f}_{pgf,i})}{\frac{\Delta V}{\nabla \cdot (\varepsilon_f \boldsymbol{\tau}) + \rho_f \varepsilon_f \mathbf{g}}} + \quad (4)$$

where ρ_f , \mathbf{u} , and P are, respectively, the fluid density, velocity, and pressure; k_c and ΔV are, respectively, the number of particles in a considered computational cell and the volume of the computational cell; and $\boldsymbol{\tau}$ is the fluid viscous stress tensor, given by

$$\boldsymbol{\tau} = (\eta_{laminar} + \eta_{turbulent})[(\nabla \mathbf{u}) + (\nabla \mathbf{u})^{-1}] \quad (5)$$

where $\eta_{laminar}$ is fluid molecular viscosity and $\eta_{turbulent} = C_\mu \rho_f k^2 / \varepsilon$ is turbulent viscosity and calculated using a standard k – ε turbulent model. Thus the turbulent kinetic energy k and dissipation rate of turbulent kinetic energy ε are governed by the k -equation:

$$\frac{\partial(\rho_f \varepsilon_f k)}{\partial t} + \nabla \cdot (\rho_f \varepsilon_f \mathbf{u} k) = \nabla \cdot \left[\varepsilon_f \left(\eta_{laminar} + \frac{\eta_{turbulent}}{\sigma_k} \right) \nabla k \right] + \varepsilon_f G_k - C_D \rho_f \varepsilon_f \varepsilon \quad (6)$$

and the ε -equation:

$$\frac{\partial(\rho_f \varepsilon_f \varepsilon)}{\partial t} + \nabla \cdot (\rho_f \varepsilon_f \mathbf{u} \varepsilon) = \nabla \cdot \left[\varepsilon_f \left(\eta_{laminar} + \frac{\eta_{turbulent}}{\sigma_\varepsilon} \right) \nabla \varepsilon \right] + \frac{\varepsilon_f \varepsilon}{k} (C_1 G_k - C_2 \rho_f \varepsilon) \quad (7)$$

where

$$G_k = \eta_{turbulent} \left(\frac{\partial u_i}{\partial x_j} + \frac{\partial u_j}{\partial x_i} \right) \frac{\partial u_i}{\partial x_j} \quad (8)$$

where u_i and u_j denote the components of gas velocity vector \mathbf{u} , x_i and x_j denote Cartesian coordinate, and the values of constants used in the k – ε turbulent model are: $C_\mu = 0.09$; $C_D = 1.00$; $C_1 = 1.44$; $C_2 = 1.92$; $\sigma_k = 1.00$; $\sigma_\varepsilon = 1.30$.⁴⁸ Modeling particle–turbulence interaction involves turbulent particle dispersion⁴⁹ and turbulent modulation⁵⁰ and is still an open research topic. To date, there is no reliable and general model available for such a purpose; for example, even for the widely studied dilute-phase pneumatic conveying, some turbulent behaviours cannot be predicted by all the existing Lagrangian or Eulerian turbulent-modulation models.^{16,51} Therefore, the interaction between particles and turbulence is not considered to avoid introducing uncertainties into this study.

2.3. Solution and Coupling Schemes. The method for numerical solution of a CFD–DEM problem has been well established in the literature. In this work, for the DEM model, an explicit time integration method is used to solve the translational and rotational motions of discrete particles.⁵² For the CFD model, the finite volume method with the SIMPLE velocity–pressure coupling method⁵³ is used to solve the governing equations for gas phase by means of nonstaggered grid arrangements in a body-fitted coordinate system.⁵⁴ The two-

Table 1. Parameters Used in the Present Simulations^a

parameter	value
<i>Pipe and Flow</i>	
pipe diameter, D (m)	0.04
pipe length, L (m)	5.0
number of body-fitted CFD cells	$8 \times 8 \times 700$
solid flow rate, w (kg/s)	0.6
gas velocity ^b , U_g (m/s)	10.0 (10.0–45.0)
solid loading ratio, SLR	7.3–33.0
<i>Gas</i>	
gas used	air
density, ρ_f (kg/m ³)	1.205
viscosity, η (kg/m/s)	1.85×10^{-5}
<i>Particles</i>	
shape	spherical
diameter, d_p (mm)	3.0
number, N	15000–42000
density, ρ_p (kg/m ³)	1000
Young's modulus, E (Pa)	1.0×10^8
Poisson ratio, ν	3.3
sliding friction coefficient, μ_s	0.3
rolling friction coefficient, μ_r	0.01
restitution, e	0.8
<i>Time</i>	
physical time simulated, s	10.0
time step, Δt (s)	5.0×10^{-6}

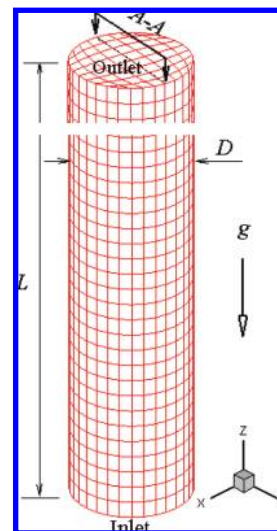
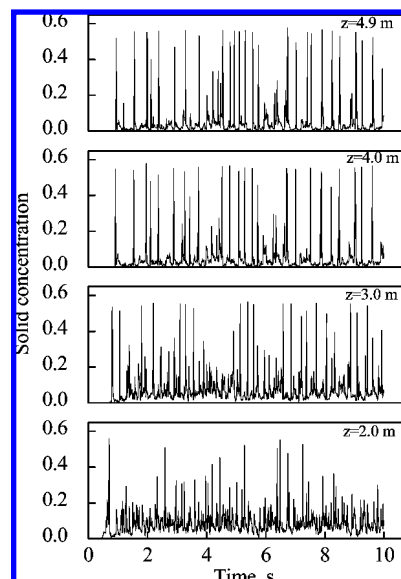
^a The wall is assumed to have the same properties as particles. ^b Base value and varying range in bracket.

way coupling of particle and fluid flows is numerically achieved as follows. At each time step, DEM will give information, such as the positions and velocities of individual particles, for the evaluation of porosity and volumetric particle–fluid forces in a computational cell. CFD will then use these data to determine the gas flow field, yielding the particle–fluid forces acting on individual particles. Incorporation of the resulting forces into DEM will produce information about the motion of individual particles for the next time step. This solution scheme has been well established since the work of Xu and Yu,²³ and is used in this work.

To accurately calculate the fluid drag forces on particles using local fluid velocity on particle position, our recently proposed point-locating scheme under 3D hybrid grids³⁶ is used to locate the host cell where a considered particle is residing, and then the fluid velocity stored on the center of the host cell is mapped to the particle position using a least-squares interpolation method. In addition, OpenMP technique applicable to computers consisting of shared-memory multiprocessors or multicore processors is used to parallelize our in-house CFD–DEM code, following the work of Henty.⁵⁵

2.4. Simulation Conditions. Table 1 shows the parameters used in the present study. To obtain phase diagram and typical flow regimes in vertical pneumatic conveying, gas velocity is varied from 10.0 to 45.0 m/s for a constant solid flow rate of 0.6 kg/m³. The resultant solid loading ratio (SLR) ranges from 7.3 to 33.0. A 3D, 5-m long vertical pipe with internal diameter of 0.04 m is chosen as the computation domain. The domain is meshed with body-fitted grids, as illustrated in Figure 1. The grid scheme $8 \times 8 \times 700$ is determined according to the grid-independence study used in a CFD study. The particles used are spherical, of diameter 3 mm, density 1000 kg/m³, restitution coefficient 0.8, corresponding to polyethylene pellets suited for slug flow and dispersed flow.⁴

In all simulations, particles are injected into the pipe from the bottom at a constant solid flow rate, and reloaded as new particles when moving out of the pipe for efficiently utilizing

**Figure 1.** Pipe geometry and CFD mesh.**Figure 2.** Temporal variations of solid concentration at different heights; $U_g = 10.0$ m/s for the transport of polyethylene pellets.

the physical memory for computation. For gas flow, a fixed uniform velocity profile at the inlet is adopted while the normal gradients of all variables at the outlet are set to zero assuming that the flow is fully developed. For DEM computation, the pipe wall is treated as rigid spheres with an infinite diameter and has no displacement and movement resulting from particle–wall interaction. A no-slip condition as used in a CFD study is applied to gas phase at the pipe wall.

Each simulation lasts for 10 s and the simulation results are recorded every 0.01 s. Because macroscopically stable flow regimes are considered in this work, the present analysis involves only simulation results under fully developed conditions, as done in most experimental studies.^{6,8,10} Figure 2 shows that when $U_g = 10.0$ m/s, the flow has almost the same solid concentration profile for $z > 4.0$ m and can thus be regarded as fully developed. On the basis of such principle, simulation data in the pipe section between $z = 4.2$ and $z = 4.7$ m at the physical time from 4 to 10 s for all simulations are chosen for the present analysis.

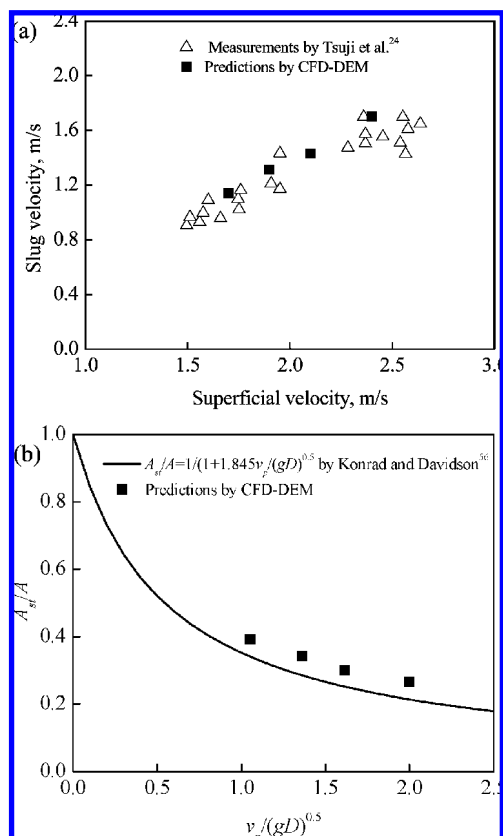


Figure 3. Prediction of the horizontal slug flow based on the experimental work of Tsuji et al.:²⁴ (a) slug velocity and (b) settled layer.

3. Results and Discussion

3.1. Model Validation. Before studying flow regimes in vertical pneumatic conveying, the validity of the present CFD-DEM model is verified using the experimental measurements reported by Tsuji et al.²⁴ and Narimatsu and Ferreira.⁹ The experimental work of Tsuji et al.²⁴ is first simulated, where particles are horizontally transported in terms of slug flow. In such a system, the velocity and height of settled layer are two key parameters characterizing particle behaviors. Figure 3a shows that slug velocity increases linearly with superficial velocity both in the predicted results and experimental measurements, and they are in a good agreement with each other. Here, particle size ($=0.003$ m) and pipe diameter ($=0.05$ m) are the same as those used in the experiments, and a 0.8 m short pipe facilitated with periodic boundary conditions for gas and solid phases in the flow direction is considered for computational efficiency. The friction coefficient and restitution coefficient are equal to 0.3 and 0.9 both for particle-particle and particle-wall interactions. These parameters and others used in this simulation are similar to those used by Tsuji et al.²⁴ who have also conducted a 1D CFD-3D DEM study of this system. Figure 3b shows the relation between the cross-sectional ratio of settled layer to pipe and the average particle velocity in a slug, predicted by the CFD-DEM simulations and the analytical model of Konrad and Davidson,⁵⁶ which has been well-recognized and widely adopted in predicting pressure drop across slugs in practical pneumatic conveying.⁵⁷ It can be seen that the numerical and analytical results reasonably agree with each other.

In the second case, the vertical transportation of glass beads in dispersed flow regime, as reported by Narimatsu and Ferreira,⁹ is simulated. For this case, the pressure drop and voidage ($= 1 -$

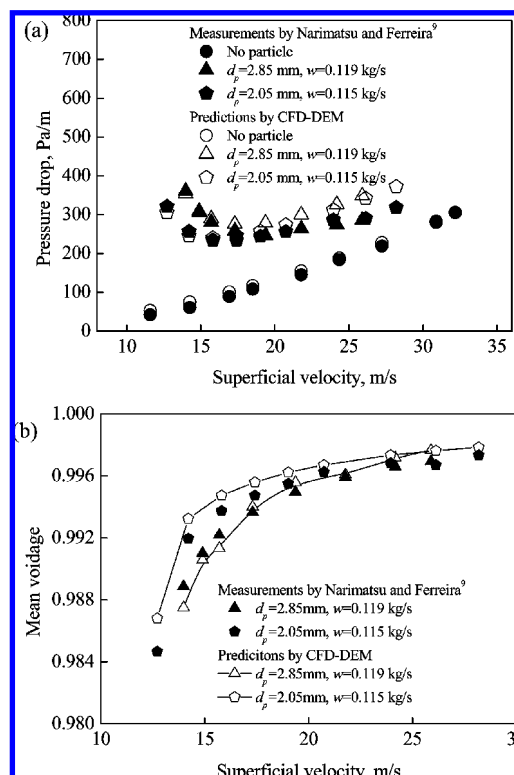


Figure 4. Prediction of the vertical transport of glass beads as compared with the measurements of Narimatsu and Ferreira:⁹ (a) pressure drop and (b) mean voidage.

solid concentration) are predicted and compared with the experimental measurements as they are the two major concerned parameters in engineering application. In this simulation, the pipe geometry ($L = 3$ m and $D = 0.0534$ m), particle size, and solid and gas flow rates shown in Figure 4 are exactly the same as those used in the experiments. The friction coefficient and restitution coefficient are equal to 0.3 and 0.6, respectively, as used in our previous CFD-DEM study of gas-solid flow in a fluidized bed.⁴⁷ It can be seen from Figure 4a that quantitative prediction of the pressure drop in the considered system can be achieved by the present model, although overpredictions are observed at relatively high gas velocities. Figure 4a also shows that the present model can satisfactorily predict the effect of particle size on pressure drop, that is, pressure drop is sensitive to particle size at relatively low gas velocities, but not at high gas velocities. Figure 4b shows that the mean voidage in the pipe sharply increases with gas velocity first, and then slows down. The experimental and numerical results reasonably agree with each other.

It should be pointed out that the CFD-DEM is not perfect, having some uncertainties related to the equations to calculate particle-particle and particle-fluid interaction forces, the selection of parameters for simulation, and so on. Nonetheless, the results shown in Figures 3 and 4 confirm that the proposed 3D CFD-DEM model can be used to describe the gas-solid flow in pneumatic conveying, at least qualitatively. Chu and Yu³⁷ reached a similar conclusion in their study of the gas-solid flow in pneumatic bends. Their approach is in essence the same as the present work, although the simulations were run under a different platform (they employed FLUENT rather than in-house code in their CFD computation). The analysis below will be based on the results produced under the conditions given in

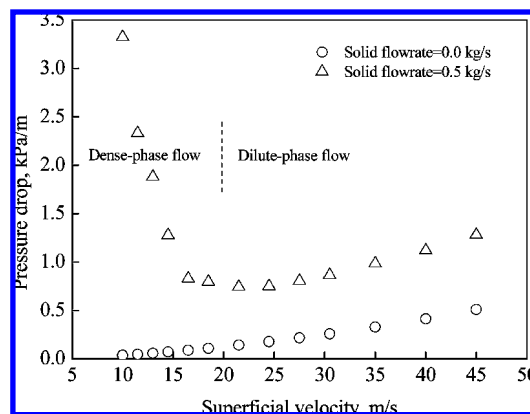


Figure 5. Pressure drop-gas velocity phase diagram for the transport of polyethylene pellets, at the locations between $z = 4.2$ m and $z = 4.7$ m.

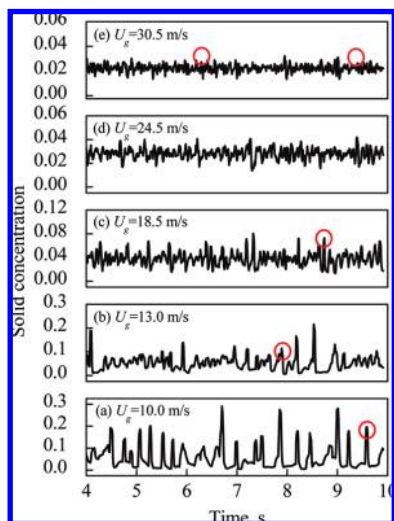


Figure 6. Temporal variations of solid concentration at the locations between $z = 4.2$ and $z = 4.7$ m at different gas velocities, corresponding to Figure 5.

section 2.4. Its aim is to understand the fundamentals underlying the gas–solid flow in different regimes in terms of the governing forces.

3.2. Flow Regimes and Flow Transition. When a material is transported in a specific system with varying gas velocities and a fixed solid flow rate, the simplest method to describe the resulting flow regimes and flow transition is the phase diagram plotting pressure drop as a function of gas velocity. Figure 5 shows such a phase diagram simulated for the vertical transport of polyethylene pellets when $SLR = 7.3–33.0$. In the figure, the pressure drops are the time-averaged values measured at the locations between $z = 4.2$ and $z = 4.7$ m. It can be seen that when gas velocity is increased, the gas-only pressure drop increases, whereas with solids loaded, the pressure drop initially decreases rapidly to a minimum and then increases gradually. The region to the right of the minimum is usually referred to as dilute-phase flow and the region to the left is called dense-phase flow. The change from dense-phase flow to dilute-phase flow is the so-called flow transition. These results qualitatively agree with the experimental measurements.^{6,14}

Figures 6–8 show the temporal variations of solid concentration and pressure drop, together with typical solid flow patterns at five gas velocities in the phase diagram (Figure 5). It can be seen that two flow modes, that is, the slug flow regime (Figure 8a–c) and the dispersed flow regime (Figure 8d,e) are numerically obtained for the vertical transport of polyethylene pellets,

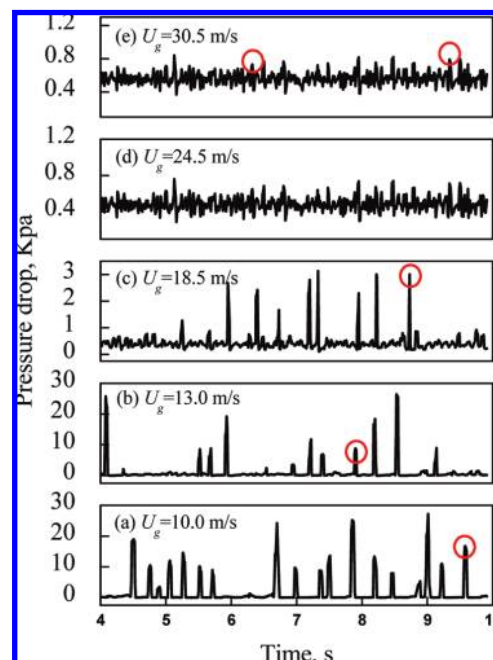


Figure 7. Temporal variations of pressure drop at the locations between $z = 4.2$ and $z = 4.7$ m at different gas velocities, corresponding to Figure 6.

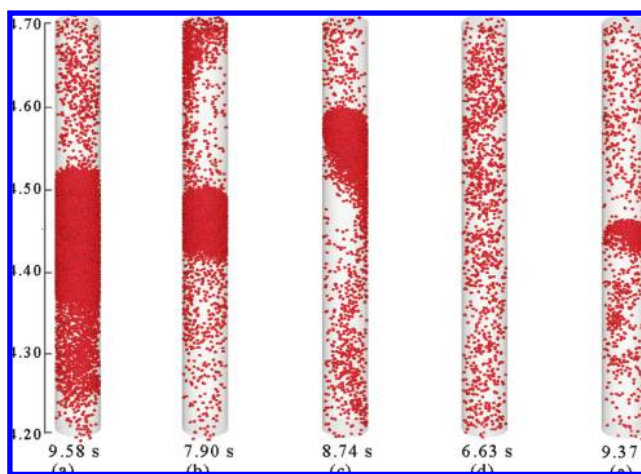


Figure 8. Snapshots showing representative particle flow patterns at different gas velocities: $U_g =$ (a) 10.0, (b) 13.0, (c) 18.5, (d) 30.5, and (e) 30.5 m/s, corresponding to different times (labeled with red circles) in Figure 6 or Figure 7.

which is consistent with the experimental results of Pan.⁴ In the slug flow regime, the entire cross area of the pipe is filled with particles in a slug, but with a very small number of particles in other parts of the pipe. As a slug moves along the pipe, some particles are observed to fall from the back of the previous slug through the air gap between slugs and be collected by the following slug, as recorded by Strauss et al.⁴⁰ using a CCD camera. In addition, a pressure drop peak and a solid concentration peak always come up when a slug passes through the considered pipe, and a large pressure drop usually corresponds to a long slug, which agrees well with the general observations of slug flow.^{58–60} It also shows that the pressure drop or slug length varies due to the unstable nature of slug flow (e.g., see Figures 6a and 7a). This phenomenon has been experimentally observed by Kawaguchi et al.⁶¹ and Li et al.,⁶⁰ but not reproduced in the previous CFD–DEM studies of slug flow with a short pipe and PBC applied. For the dispersed flow

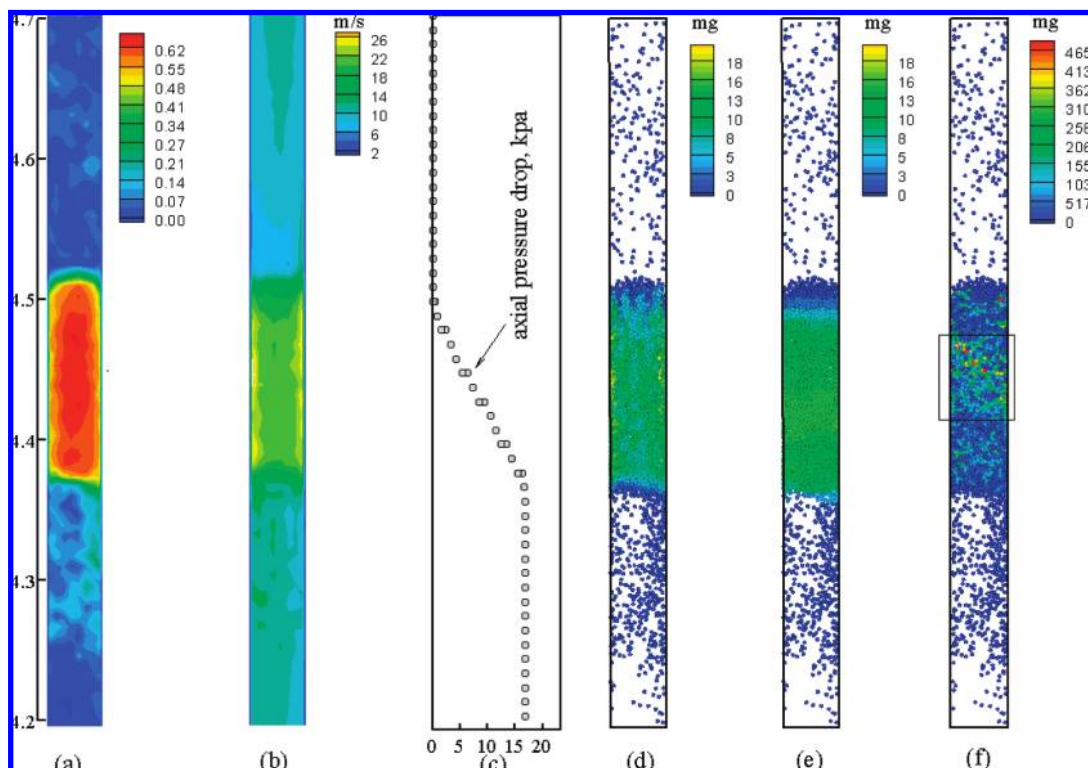


Figure 9. Snapshots showing the spatial distributions of forces on particles and the related flow properties on the A–A sectional plane for the slug flow regime: (a) solid concentration; (b) axial gas velocity; (c) axial pressure drop along the pipeline; (d) axial fluid drag force; (e) axial pressure gradient force; (f) normal contact force, corresponding to Figure 8a. In this figure (and Figures 10, 11 and 16), mg denotes the gravity of a particle and is the units of the forces shown.

regime, particles are distributed throughout the entire pipe (Figure 8d), with some clusters (Figure 8e) being observed from time to time due to the high solid loading used, and there are no large pressure drop peaks observed in the slug flow regime.

Figures 6–8 also demonstrate how the slug regime transits into the dispersed flow regime. When the gas velocity is increased in the range from 10.0 to 18.5 m/s where the flows belong to the slug flow regime, slug length decreases (Figure 8a–c). This leads to reduced average pressure drop and pressure fluctuation peak (Figure 7a–c). At $U_g = 18.5$ m/s, which corresponds to the flow transition observed in Figure 5, slugs become unstable, featured with an asymmetrical shape (Figure 8c). At higher gas velocities, slugs are dissolved by strong gas stream, particles are hence dispersed into the entire pipe and form some small clusters (Figure 8d,e), and the flow is developed into the dispersed flow regime which is generally known as a stable flow mode characterized by relatively uniform pressure fluctuations (see Figure 7d). If the gas velocity is increased further, the size and number of clusters decrease, the flow becomes more homogeneous, and the average pressure drop increases although pressure fluctuations are still uniform (Figure 7e). It is noted that some clusters (e.g., see Figure 8e) in the dilute-phase flow sometimes look like small slugs. This results in the difficulty that the flow transition defined in the phase diagram shown in Figure 5 can hardly be visually identified from the evolution of particle flow pattern. In fact, such difficulty can be pronounced when solid loading is low. For example, in the work of Narimatsu and Ferreir,⁹ the flows when $SLR < 3.5$ had a transition in the pressure drop–gas velocity phase diagram (Figure 4a), but only dispersed flow regime was observed. This indicates the limitation of visualized particle patterns in identifying flow regimes, or the inconsistency between the pressure drop–gas velocity phase diagram and the observation of solid flow patterns.

3.3. Force Analysis. As indicated by eqs 1 and 2, the motion of a particle is governed by various particle–particle, particle–wall, particle–fluid, and gravity forces. Analysis of these forces should hence generate some insight into particles behavior, leading to a better understanding of flow regimes and flow transition. Such analysis is difficult to achieve experimentally but can be readily performed based on the present CFD–DEM simulations. In the following, we will first establish a general picture about the forces acting on particles in vertical pneumatic conveying, then discuss the roles of these forces in the pressure drop–gas velocity phase diagram, and finally propose new phase diagrams in terms of these forces.

3.3.1. Key Features of the Forces on Particles. Figures 9–11 show the calculated forces and relevant flow information at three representative gas velocities, namely $U_g = 10.0$ m/s for the slug flow regime, 18.5 m/s for the flow transition, and 30.5 m/s for the dispersed flow regime. For clarity, here only the A–A section plane (Figure 1) with a thickness 4 particle diameters is considered, and the side view is shown. The results in the figures include the spatial distributions of solid concentrations, axial gas velocities, gas pressure drop along the pipeline, axial fluid drag forces, axial pressure gradient forces, and particle–particle forces. They are corresponding to particle configures at different times. Here the radial results, which are small and do not account for the transport of particles along the pipeline, are not considered for brevity, and the magnitudes of the forces shown are expressed relative to the gravity force of a particle.

It can be seen from Figure 9a that in the slug flow regime, particles inside a slug are densely packed, with solid concentration equal to 0.58 near the center of the pipe and a slightly lower value near the walls. In contrast, solid concentration outside the slug is < 0.15 . Correspondingly, the axial gas velocity

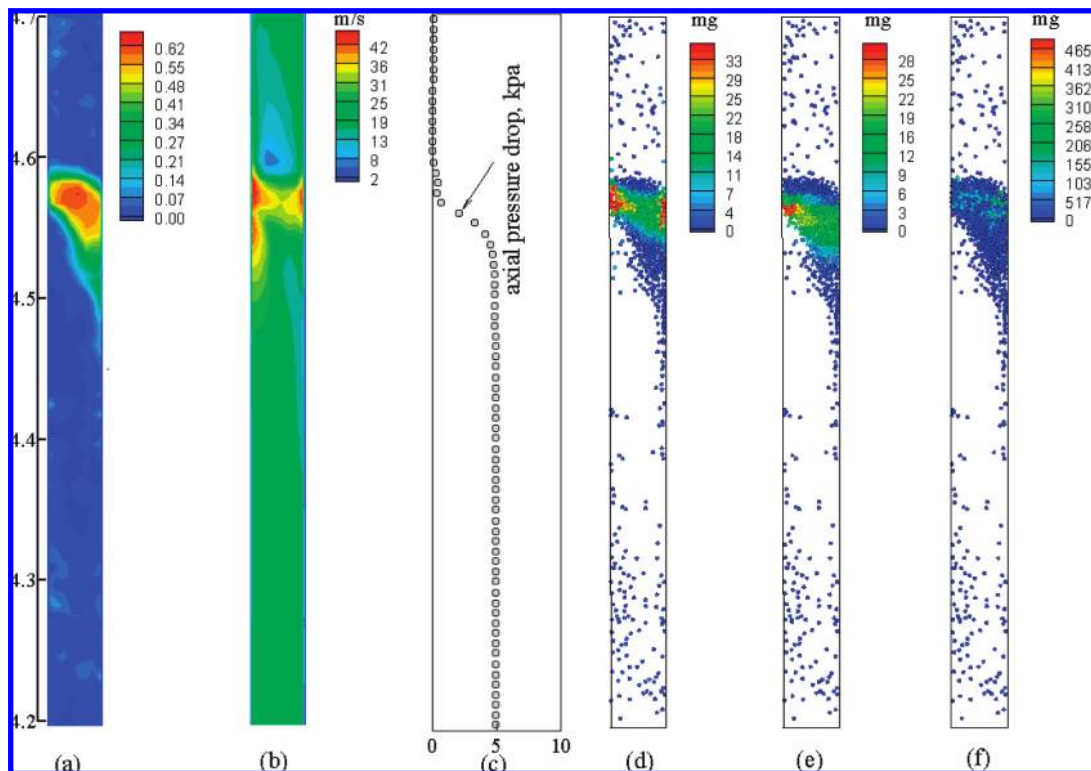


Figure 10. Snapshots showing the spatial distributions of forces on particles and the related flow properties on the A–A sectional plane for the flow transition: (a) solid concentration; (b) axial gas velocity; (c) axial pressure drop along the pipeline; (d) axial fluid drag force; (e) axial pressure gradient force; (f) normal contact force, corresponding to Figure 8c.

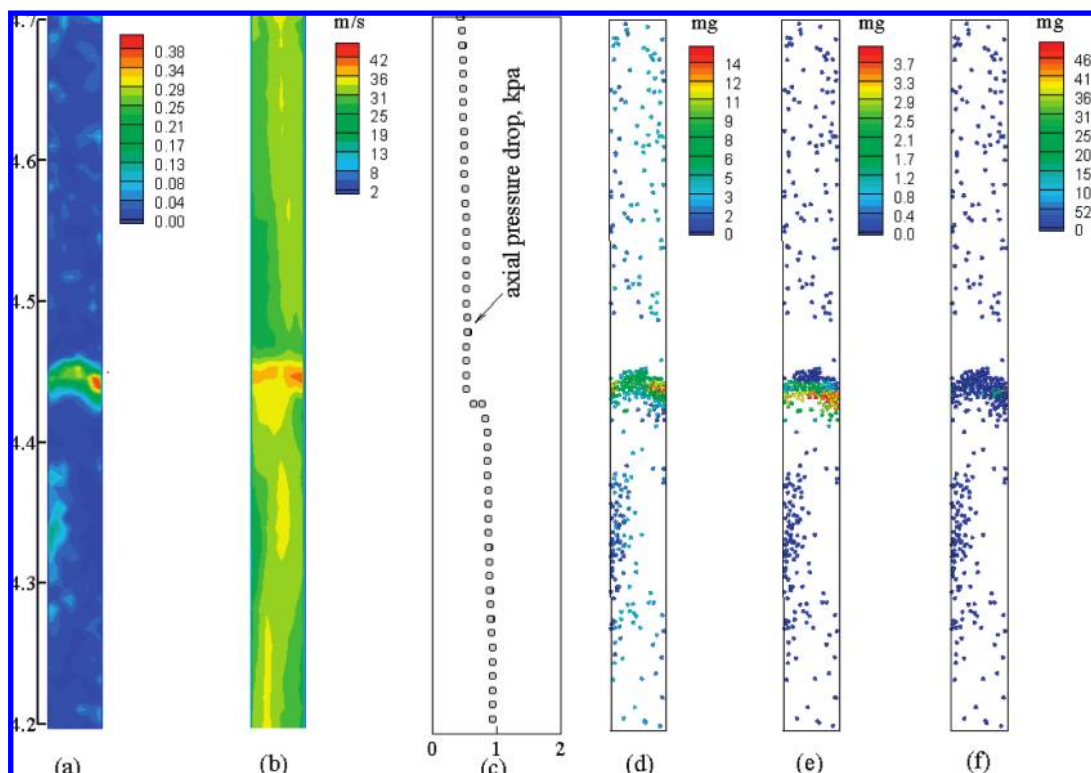


Figure 11. Snapshots showing the spatial distributions of forces on particles and the related flow properties on the A–A sectional plane for the dispersed flow regime: (a) solid concentration; (b) axial gas velocity; (c) axial pressure drop along the pipeline; (d) axial fluid drag force; (e) axial pressure gradient force; (f) normal contact force, corresponding to Figure 8e.

inside the slug is larger than those outside the slug, with a maximum near the wall and a minimum near the center of the pipe, as shown in Figure 9b. In addition, a linear pressure drop inside the slug, together with a negligible pressure drop outside

the slug is observed (Figure 9c), similar to that observed by Borzone and Klinzing.⁵⁹ Because of the above flow properties, the fluid drag force shown in Figure 9d and the pressure gradient force shown in Figure 9e are both several times the particle

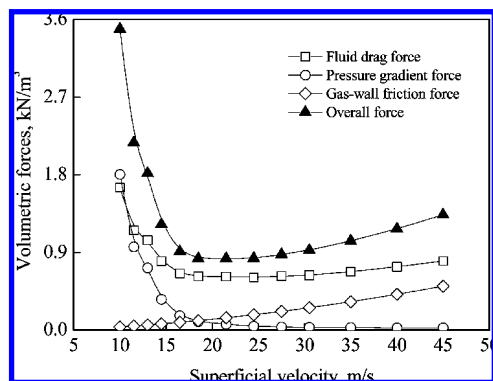


Figure 12. Average volumetric fluid drag force, pressure gradient force and gas-wall friction force as a function of gas velocity.

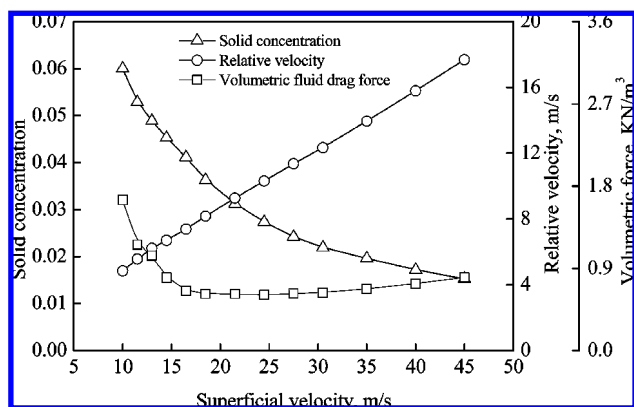


Figure 13. Average solid concentration and relative velocity of gas to particle as a function of gas velocity.

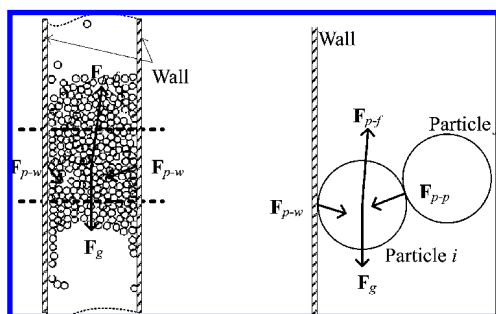


Figure 14. Schematic illustration of force analysis conducted at a pipe scale (a) and a particle scale (b).

gravity force inside the slug and less than particle gravity force outside the slug. Interestingly, it is found that the pressure gradient force has a uniform distribution in the radial direction, different from the fluid drag force. Moreover, different from the particle-fluid forces, the particle-particle force (Figure 9f) is mainly distributed near the middle section of the slug, and can be a thousand times the particle gravity force. Here, the particle-particle force is the normal contact force which is the major particle-particle force resulting from the interactions between particles.

Figure 10 shows that at the flow transition, the trends of solid concentration, gas velocity, and gas pressure drop are generally similar to those observed in Figure 9 as the flow is still a slug flow. The slug has a very small region with high solid concentration and thus tends to collapse. This is attributed to the instability of slugs at the flow transition, which may lead to nonuniform radial distribution of the fluid drag forces and pressure gradient forces. It can be seen that for the flow

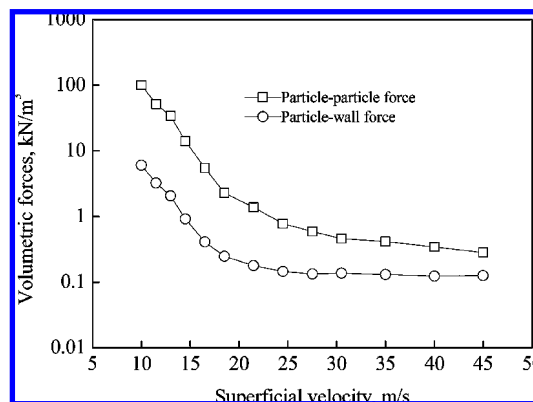


Figure 15. Average volumetric particle-particle and particle-wall forces as a function of gas velocity.

transition, the fluid drag force and the pressure gradient force are still large inside the slug, with values close to those in Figure 9, and small outside the slug. However, the normal contact forces inside the slug decrease evidently.

Figure 11 shows that in the dispersed flow regime, a cluster is very different from a slug, having much lower solid concentration, although it may look like a small slug. Sharp increases of gas velocity and pressure drop at the location of a cluster are observed in Figure 11. Except for these sharp changes, the pressure drop is found to linearly decrease gradually along the pipeline, as experimentally observed in the dilute-phase conveying.⁹ Therefore, particles in clusters undertake large fluid drag forces and pressure gradient forces compared to other particles. It is shown that in the dispersed flow regime, the magnitude of the fluid drag forces is now greater than that of particle gravity force due to high gas velocity (Figure 11d), and the pressure gradient forces still remain less than particle gravity forces except for those in a cluster (Figures 11e). Moreover, particle-particle interaction cannot be evidently observed, even in clusters, as shown in Figure 11f. Note that for loose clusters in the dispersed flow regime, there are no obvious jump of gas velocity, pressure drop, and particle-fluid force.

3.3.2. Roles of the Forces in the Pressure Drop-Gas Velocity Phase Diagram. One of the most popular mathematical methods in calculating the pressure drop in pneumatic conveying is by splitting the pressure drop into two components: gas-only pressure drop, and pressure drop due to the presence of solid particles, and then modeling them separately.⁶² These two pressure drops correspond to the gas-wall friction force and the particle-fluid force, respectively. Therefore, such forces are used to understand the behavior of pressure drop shown in the phase diagram (Figure 5). To be quantitative in the analysis, the average volumetric particle-fluid force over a period of time is introduced in this work, calculated by

$$\frac{1}{\Delta t} \sum_{\Delta t} \left[\frac{1}{V_{\text{section}}} \left(\sum_{i=1}^{N_{p,\text{section}}} \mathbf{f}_i \right) \right] \quad (9)$$

where \mathbf{f}_i represents the fluid drag force or pressure gradient force acting on particle i , $N_{p,\text{section}}$ and V_{section} are the number of particles in a considered pipe section and the volume of the pipe section, respectively.

Figure 12 shows the average volumetric fluid drag force, pressure gradient force, gas-wall friction force, and the sum of the three forces as a function of gas velocity. Here, the volumetric gas-wall friction force is estimated by the pressure drop of gas flow in an empty pipe, as done in the development

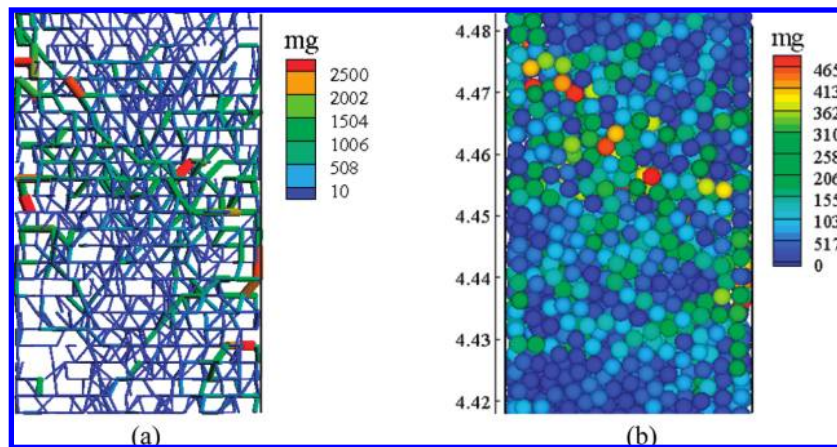


Figure 16. Force propagation through particle–particle interaction in a slug corresponding to Figure 9f (squared region), in terms of (a) force per contact, given by $|f_{cn,ij}|$; and (b) force per particle, given by $\sum_{j=1}^k |f_{cn,ij}|$.

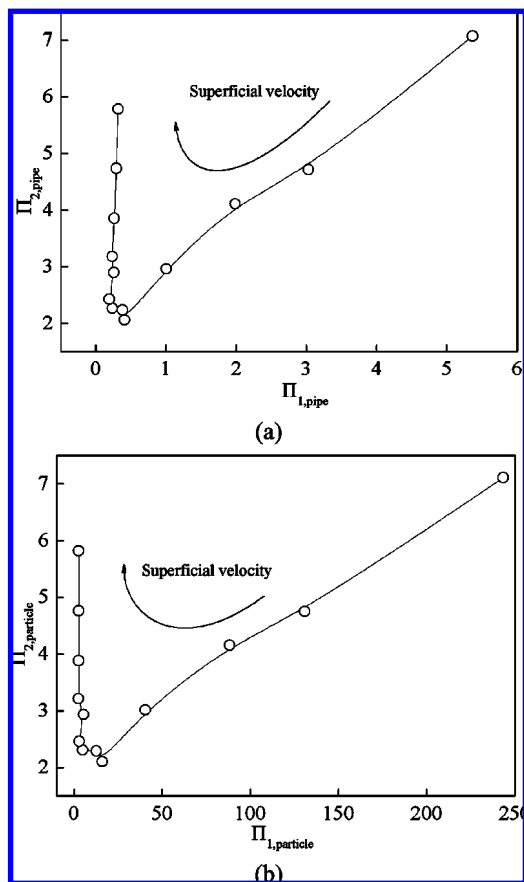


Figure 17. Phase diagram in terms of the forces on particles (a) at the pipe scale and (b) at the particle scale.

of a mathematical model for pressure prediction.⁶² It can be seen from Figure 12 that as gas velocity is increased, the fluid drag force rapidly decreases to a minimum and then slightly increases. The pressure gradient force rapidly decreases and then approaches zero. On the other hand, the gas–wall friction force increases almost linearly. It appears that these three forces alone cannot be used to identify the flow transition in the phase diagram shown in Figure 5. However, it is found that their sum initially decreases rapidly to a minimum point and then increases gradually. The trend is exactly the same as that observed in the phase diagram. This suggests that the phase diagram can be well explained in terms of the particle–fluid force and gas–wall friction force.

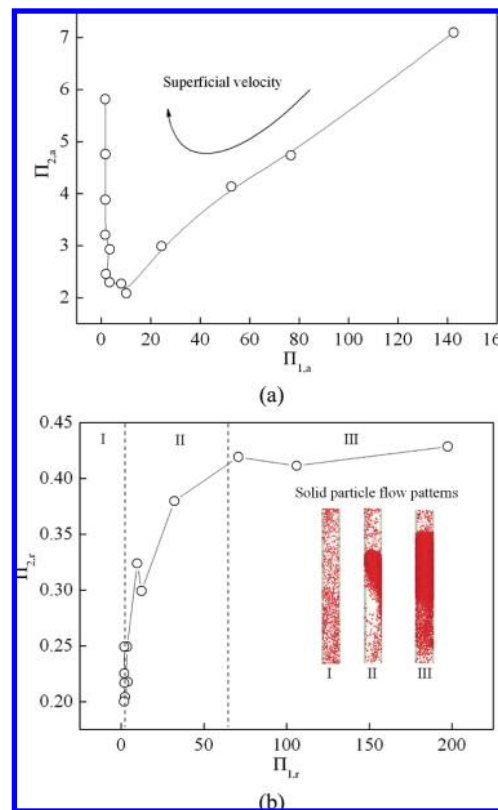


Figure 18. Phase diagram in terms of the axial (a) and radial (b) forces at the particle scale, with the inset showing the solid flow patterns in regions I, II, and III.

In fact, Figure 12 also shows how different forces affect the pressure behavior in different flow regimes. Under the present simulation conditions, for the dense-phase flow, the pressure drop is dominantly dependent on the particle–fluid force consisting of the fluid drag force and pressure gradient force, and the gas–wall friction force is negligible. Whereas for the dilute-phase flow, the pressure drop is controlled by the fluid drag force and the gas–wall friction force, and the pressure gradient force is negligible. Moreover, the rapid decrease of pressure drop in the dense-phase flow regime is attributed to the sharp decrease of the particle–fluid force. On the other hand, the increase of gas–wall friction force mainly accounts for the increase of pressure drop in the dilute-phase flow regime.

The fluid drag force can be further analyzed in relation to the gas and solid flow structure. By definition, it is a function

of solid concentration and relative velocity between gas and particle. Figure 13 show how the two factors vary with gas velocity. Here the average relative velocity over a period of time is calculated by

$$\frac{1}{\Delta t} \sum_{\Delta t} \left\{ \frac{1}{N_{\text{section}}} \left[\sum_{i=1}^{N_{p,\text{section}}} (\mathbf{u}_i - \mathbf{v}_i) \right] \right\} \quad (10)$$

It can be seen from the figure that with increasing gas velocity, the relative velocity increases linearly, whereas solid concentration rapidly decreases first and then slows down. Similar to particle flow pattern, neither solid concentration nor relative velocity alone can be used to identify the flow transition shown in Figure 5. Nonetheless, Figure 13 manifests that the fluid drag force is mainly dependent on solid concentration in the dense-phase flow and thus decreases with the decrease of solid concentration. However, for the dilute-phase flow, the effects of solid concentration and relative velocity on the fluid drag force largely counteract each other, which yielding a small change in the fluid drag force with increasing gas velocity.

3.3.3. Phase Diagram in Terms of the Forces. The phase diagram shown in Figure 5 focuses on pressure drop which is related to gas phase only. It indirectly reflects how a gas–solid flow behaves in pipelines. Consequently, such a diagram may not correspond well to visualized particle flow pattern and have limitations in application, as discussed above. To overcome this problem, we have made an attempt to use the forces governing particles motion to directly describe particle behavior in pneumatic conveying. That is, we try to establish a new phase diagram in terms of the forces governing the particle flow.

Following our recent work on pneumatic conveying,²⁹ we analyze particle–particle, particle–fluid and particle–wall forces at two scales: pipe scale and particle scale, as schematically demonstrated in Figure 14. The pipe-scale analysis considers forces acting on a sectional pipe, whereas the particle-scale analysis focuses on forces acting on an individual particle. At the pipe scale, the volumetric average particle–particle force over a period of time can be calculated by

$$|\mathbf{F}|_{\text{pipe}} = \left| \frac{1}{\Delta t} \sum_{\Delta t} \left\{ \frac{1}{V_{\text{section}}} \left[\sum_{i=1}^{N_{p,\text{section}}} \left(\sum_{j=1}^{k_i} \mathbf{f}_{\text{cn},ij} + \mathbf{f}_{\text{dn},ij} + \mathbf{f}_{\text{ct},ij} + \mathbf{f}_{\text{dt},ij} \right) \right] \right\} \right| \quad (11)$$

The force, as an internal interaction within a particle assembly, is equal to zero because they can be canceled out according to Newton's third law of motion. However, this does not hold for the particle–particle force at a particle scale, which is expressed as

$$|\mathbf{F}|_{\text{particle}} = \frac{1}{\Delta t} \sum_{\Delta t} \left\{ \frac{1}{V_{\text{section}}} \left[\sum_{i=1}^{N_{p,\text{section}}} \left(\sum_{j=1}^{k_i} |\mathbf{f}_{\text{cn},ij} + \mathbf{f}_{\text{dn},ij} + \mathbf{f}_{\text{ct},ij} + \mathbf{f}_{\text{dt},ij}| \right) \right] \right\} \quad (12)$$

Equation 12 can also apply to the calculation of the particle–wall interaction force, with particle j replaced by wall. Figure 15 shows the so obtained volumetric average particle–particle and particle–wall forces. To be consistent, the sectional pipe considered here is the same as that used in the above discussions. It can be seen from the figure that as gas velocity increases, the particle-scale particle–particle force rapidly decreases and then slows down. Interestingly, the particle–wall

force is observed to have a similar trend as the particle–particle force at relatively low gas velocities, but become almost a constant at relatively high gas velocities. The result indicates that when gas velocity is increased, the particle–wall force is first dependent on the particle–particle force; however, this dependence becomes smaller and smaller. This can be explained as follows. At relatively low gas velocities, the flows belong to the slug flow regime, and the particle–particle interactions inside a slug can be propagated toward the pipe wall, as demonstrated in Figure 16. Note that in Figure 16a each stick represents the connection of two particle centers and its thickness represents the magnitude of the normal contact force between them, and Figure 16b represents the sum (in magnitude) of the normal contact forces acting on particle i imposed by its neighboring particles. So one represents the interaction force per contact, and another the interaction force per particle. Interestingly, both figures give the same message about force propagation. At the relatively high gas velocities, the flows are dominated by the dispersed flow regime where there are only a very small number of particles contacting with each other, as shown in Figure 11f. Consequently, the force network among particles like those shown in Figure 16 cannot be established and the particle–wall forces just result from the occasional collisions of particles on pipe walls.

The forces on a particle or a particle assembly can be generally classified into three types. They are the particle–fluid force which is here the sum of the fluid drag and pressure gradient forces, the particle–particle and particle–wall forces (the two are grouped together because they behave similarly and are of the same nature), and the gravity force. This will produce two dimensionless numbers, Π_1 and Π_2 , given by

(a) at the pipe scale:

$$\Pi_{1,\text{pipe}} = \frac{\left| \frac{1}{\Delta t} \sum_{\Delta t} \left\{ \frac{1}{V_{\text{section}}} \left[\sum_{i=1}^{N_{p,\text{section}}} \left(\sum_{j=1}^{k_i+k_w} \mathbf{f}_{\text{cn},ij} + \mathbf{f}_{\text{dn},ij} + \mathbf{f}_{\text{ct},ij} + \mathbf{f}_{\text{dt},ij} \right) \right] \right\} \right|}{\frac{1}{\Delta t} \sum_{\Delta t} \left[\frac{1}{V_{\text{section}}} \left(\sum_{i=1}^{N_{p,\text{section}}} m \mathbf{g}_i \right) \right]} \quad (13a)$$

and

$$\Pi_{2,\text{pipe}} = \frac{\left| \frac{1}{\Delta t} \sum_{\Delta t} \left[\frac{1}{V_{\text{section}}} \left(\sum_{i=1}^{N_{p,\text{section}}} \mathbf{f}_{\text{drag},i} + \mathbf{f}_{\text{pgf},i} \right) \right] \right|}{\frac{1}{\Delta t} \sum_{\Delta t} \left[\frac{1}{V_{\text{section}}} \left(\sum_{i=1}^{N_{p,\text{section}}} m \mathbf{g}_i \right) \right]} \quad (13b)$$

(b) at the particle scale:

$$\Pi_{1,\text{particle}} = \frac{\frac{1}{\Delta t} \sum_{\Delta t} \left\{ \frac{1}{V_{\text{section}}} \left[\sum_{i=1}^{N_{p,\text{section}}} \left(\sum_{j=1}^{k_i+k_w} |\mathbf{f}_{\text{cn},ij} + \mathbf{f}_{\text{dn},ij} + \mathbf{f}_{\text{ct},ij} + \mathbf{f}_{\text{dt},ij}| \right) \right] \right\}}{\frac{1}{\Delta t} \sum_{\Delta t} \left[\frac{1}{V_{\text{section}}} \left(\sum_{i=1}^{N_{p,\text{section}}} m \mathbf{g}_i \right) \right]} \quad (14a)$$

and

$$\Pi_{2,\text{particle}} = \frac{\frac{1}{\Delta t} \sum_{\Delta t} \left[\frac{1}{V_{\text{section}}} \left(\sum_{i=1}^{N_{p,\text{section}}} |\mathbf{f}_{\text{drag},i} + \mathbf{f}_{\text{pgf},i}| \right) \right]}{\frac{1}{\Delta t} \sum_{\Delta t} \left[\frac{1}{V_{\text{section}}} \left(\sum_{i=1}^{N_{p,\text{section}}} m \mathbf{g}_i \right) \right]} \quad (14b)$$

Figure 17 show the new phase diagram in terms of the two dimensionless numbers. It can be seen from the figure that no matter at a pipe scale or a particle scale, the new phase diagrams can have the same message: there are two regions which correspond to the two flow regimes, that is, dense-phase flow and dilute-phase flow, the particle–particle or particle–wall interaction is almost constant at the smallest value in the dilute-phase flow but increases with the increase of Π_2 in the dense-phase flow, and the transition between the two regimes occurs when Π_1 is at its minimum. Figures 5 and 17 are consistent with each other. But the phase diagram established in terms of forces can better represent the underlying fundamentals. For example, the new phase diagram highlights an important characteristic of a dilute-phase flow, that is, the particle–particle and particle–wall forces are small, if not negligible, compared to those in a dense-phase flow. Established in terms of dimensionless numbers, it also has a potential to be used generally. This will be explored further in our planned future work.

Particles in a pipeline have axial and radial motions. Consequently, they have radial and axial interactions with wall. In recent years, different stress sensors have been developed to measure axial and radial particle–wall interaction for better understanding pneumatic conveying.^{41,43,63} In connection with such efforts, we also give new phase diagrams in terms of the axial and radial forces, as illustrated in Figure 18. Here Π_1 and Π_2 are at the particle scale, calculated according to eqs 14a and 14b but with respect to the axial and radial force components, respectively. The phase diagram based on the axial forces shown in Figure 18a is similar to that based on the total forces shown in Figure 17b. This is in line with the fact the transport of particles in a vertical pipeline is dominated by the axial forces, as well recognized in the literature.⁶⁴ However, as shown in Figure 18b, the radial particle–wall and particle–particle forces are larger than those in the axial direction. This is expected according to the Coulomb's friction law.

It is however of interest to note that different from Figure 18a and other phase diagrams, Figure 18b gives three regions. In region I, $\Pi_{1,r}$ is low and almost independent of $\Pi_{2,r}$, which obviously corresponds to the dilute-phase flow regime. In region III, $\Pi_{2,r}$ is large and does not change much with $\Pi_{1,r}$. This region corresponds to slug flow where particles are densely packed and hence the interaction between particles and fluid gradually reaches its maximum. In region II, $\Pi_{2,r}$ increases with the increase of $\Pi_{1,r}$. This region shows a transition between dispersed flow and slug flow, and its combination of region III gives the dense-phase flow regime.

4. Conclusions

A 3D CFD–DEM model has been developed and used to study the flow regimes in vertical pneumatic conveying. The results from the present work can be summarized below:

(1) The proposed numerical model is a valid method in the study of pneumatic conveying. It can satisfactorily capture the key flow behaviors observed, such as particle flow pattern and

gas pressure characteristics. Particularly, it can reproduce the transition from slug flow to dispersed flow with the increase of velocity.

(2) The mechanisms underlying the relationship between pressure drop and gas velocity have been analyzed. It is shown that the decrease of pressure drop in the dense-phase flow results from the decreases of fluid drag force and pressure gradient force, and the increase of pressure drop in the dilute-phase flow can be attributed to the increases of fluid drag force and gas-wall friction force.

(3) The forces governing the flow of particles have been analyzed at the pipe and particle scales, resulting in the establishment of new phase diagrams to identify the dilute-phase and dense-phase flow regimes. The particle–particle and/or particle–wall force increases with the increase of the particle–fluid force in the dense-phase flow, but is small, if not negligible, in the dilute-phase flow. Moreover, the phase diagram based on the radial forces can also lead to the identification of dispersed and slug flows, and the transient flow in-between.

Finally, it should be pointed out that flow regimes also depend on material properties, solid flow rate, and pipe geometries in addition to gas velocity. It is important to understand the effects of the pertinent variables in order to produce results useful in practice. Some work in this direction is underway, and the results will be reported in the future.

Acknowledgment

The authors are grateful to the Australia Research Council (ARC) for the financial support of this work and the Australian Centre for Advanced Computing and Communications (AC3) for the use of its computational facilities.

List of Symbols

- A = area
- a = fraction volume of a particle
- c_{d0} = fluid drag coefficient on a isolated particle.
- C_μ = empirical constant (0.09)
- C_D = empirical constant (1.00)
- C_1 = empirical constant (1.44)
- C_2 = empirical constant (1.92)
- d = particle diameter, m
- D = diameter of pipe
- E = Young's modulus, Pa
- \mathbf{f} = particle scale forces, N
- \mathbf{F} = volumetric force, $\text{N} \cdot \text{m}^{-3}$
- G = production of turbulent kinetic energy
- g = gravitational acceleration, $\text{m} \cdot \text{s}^{-2}$
- I = moment of inertia of particle, $\text{kg} \cdot \text{m}^2$
- k = turbulent kinetic energy
- k_c = number of particles in a considered computation cell
- k_i = number of particles in contact with particle
- k_w = number of walls in contact with particle i
- L = length of pipe, m
- \mathbf{T} = torque, $\text{N} \cdot \text{m}$
- m = mass of particle, kg
- N = number of particles
- P = pressure, Pa
- $\Delta \mathbf{r}$ = vector from cell center to particle center position, m
- \mathbf{R} = vector from the mass center of the particle to the contact point, m
- SLR = solid loading ratio
- t = time, s
- Δt = time step, s

\mathbf{v} = particle translational velocity, $\text{m}\cdot\text{s}^{-1}$
 v_p = particle velocity in a slug, $\text{m}\cdot\text{s}^{-1}$
 V = volume, m^3
 \mathbf{u} = gas velocity, $\text{m}\cdot\text{s}^{-1}$
 u_i = the component of the velocity vector \mathbf{u}
 U = superficial velocity, $\text{m}\cdot\text{s}^{-1}$
 w = mass flow rate, $\text{kg}\cdot\text{s}^{-1}$
 x_i = Cartesian coordinate

Greek

ε = dissipation of turbulent kinetic energy
 ε_f = porosity
 γ = damping coefficient
 η = gas viscosity, $\text{kg}\cdot\text{m}^{-1}\cdot\text{s}^{-1}$
 ρ = density, $\text{kg}\cdot\text{m}^{-3}$
 ω = particle angular velocity, s^{-1}
 $\hat{\omega}$ = unit vector defined by $\hat{\omega} = \omega/|\omega|$
 μ = friction coefficient
 ν = Poisson ratio
 σ_k = empirical constant (1.00)
 σ_ε = empirical constant (1.30)
 $\boldsymbol{\tau}$ = fluid viscous stress tensor, $\text{kg}\cdot\text{m}^{-1}\cdot\text{s}^{-2}$

Subscripts

a = axial
c = contact
cell = computational cell
d = damping
drag = fluid drag force
f = fluid
i = particle i
ij = between particles i and j
j = particle j
n = normal component
p = particle
pgf = pressure gradient force
r = rolling friction
s = sliding
section = pipe section
st = settled layer of horizontal slug flow
t = tangential component

Literature Cited

- (1) Mills, D. *Pneumatic Conveying Design Guide*; Butterworths: London, U.K., 2004.
- (2) Wypych, P. W.; Yi, J. L. Minimum transport boundary for horizontal dense-phase pneumatic conveying of granular materials. *Powder Technol.* **2003**, *129*, 111.
- (3) Albion, K.; Briens, L.; Briens, C.; Berruti, F.; Book, G. Flow regime determination in upward inclined pneumatic transport of particulates using non-intrusive acoustic probes. *Chem. Eng. Process.* **2007**, *46*, 520.
- (4) Pan, R. Material properties and flow modes in pneumatic conveying. *Powder Technol.* **1999**, *104*, 157.
- (5) Dhodapkar, S. V.; Klinzing, G. E. Pressure-fluctuations in pneumatic conveying systems. *Powder Technol.* **1993**, *74*, 179.
- (6) Matsumoto, S.; Harakawa, H. Statistical-analysis of the transition of the flow pattern in vertical pneumatic conveying. *Int. J. Multiphase Flow* **1987**, *13*, 123.
- (7) Wen, C. Y.; Simons, H. P. Flow characteristics in horizontal fluidized solids transport. *AIChE J.* **1959**, *5*, 263.
- (8) Rao, S. M.; Zhu, K. W.; Wang, C. H.; Sundaresan, S. Electrical capacitance tomography measurements on the pneumatic conveying of solids. *Ind. Eng. Chem. Res.* **2001**, *40*, 4216.
- (9) Narimatsu, C. P.; Ferreira, M. C. Vertical pneumatic conveying in dilute and dense-phase flows: Experimental study of the influence of particle density and diameter on fluid dynamic behavior. *Braz. J. Chem. Eng.* **2001**, *18*, 221.
- (10) Tsuji, Y.; Morikawa, Y. Flow pattern and pressure fluctuation in air-solid two-phase flow in a pipe at low air velocities. *Int. J. Multiphase Flow* **1982**, *8*, 329.
- (11) Pakh, J. B.; Klinzing, G. E. Assessing flow regimes from pressure fluctuations in pneumatic conveying of polymer pellets. *Part. Sci. Technol.* **2008**, *26*, 247.
- (12) Zhu, K. W.; Rao, S. M.; Wang, C. H.; Sundaresan, S. Electrical capacitance tomography measurements on vertical and inclined pneumatic conveying of granular solids. *Chem. Eng. Sci.* **2003**, *58*, 4225.
- (13) Jones, M. G.; Williams, K. C. Predicting the mode of flow in pneumatic conveying systems-a review. *Particuology* **2008**, *6*, 289.
- (14) Molerus, O. Overview: Pneumatic transport of solids. *Powder Technol.* **1996**, *88*, 309.
- (15) Hadinoto, K.; Jones, E. N.; Yurteri, C.; Curtis, J. S. Reynolds number dependence of gas-phase turbulence in gas-particle flows. *Int. J. Multiphase Flow* **2005**, *31*, 416.
- (16) Hadinoto, K.; Curtis, J. S. Numerical simulation of the Reynolds number effect on gas-phase turbulence modulation. *Int. J. Multiphase Flow* **2009**, *35*, 129.
- (17) Hadinoto, K.; Curtis, J. S. Effect of interstitial fluid on particle-particle interactions in kinetic theory approach of dilute turbulent fluid-particle flow. *Ind. Eng. Chem. Res.* **2004**, *43*, 3604.
- (18) Lee, L. Y.; Quek, T. Y.; Deng, R. S.; Ray, M. B.; Wang, C. H. Pneumatic transport of granular materials through a 90 degrees bend. *Chem. Eng. Sci.* **2004**, *59*, 4637.
- (19) Levy, A. Two-fluid approach for plug flow simulations in horizontal pneumatic conveying. *Powder Technol.* **2000**, *112*, 263.
- (20) Henthorn, K. H.; Park, K.; Curtis, J. S. Measurement and prediction of pressure drop in pneumatic conveying: Effect of particle characteristics, mass loading, and Reynolds number. *Ind. Eng. Chem. Res.* **2005**, *44*, 5090.
- (21) Huber, N.; Sommerfeld, M. Modelling and numerical calculation of dilute-phase pneumatic conveying in pipe systems. *Powder Technol.* **1998**, *99*, 90.
- (22) Yilmaz, A.; Levy, E. K. Formation and dispersion of ropes in pneumatic conveying. *Powder Technol.* **2001**, *114*, 168.
- (23) Xu, B. H.; Yu, A. B. Numerical simulation of the gas-solid flow in a fluidized bed by combining discrete particle method with computational fluid dynamics. *Chem. Eng. Sci.* **1997**, *52*, 2785.
- (24) Tsuji, Y.; Tanaka, T.; Ishida, T. Lagrangian numerical-simulation of plug flow of cohesionless particles in a horizontal pipe. *Powder Technol.* **1992**, *71*, 239.
- (25) Zhu, H. P.; Zhou, Z. Y.; Yang, R. Y.; Yu, A. B. Discrete particle simulation of particulate systems: Theoretical developments. *Chem. Eng. Sci.* **2007**, *62*, 3378.
- (26) Tsuji, Y. Multi-scale modeling of dense phase gas-particle flow. *Chem. Eng. Sci.* **2007**, *62*, 3410.
- (27) Van der Hoef, M. A.; Annaland, M. V.; Deen, N. G.; Kuipers, J. A. M. Numerical simulation of dense gas-solid fluidized beds: A multiscale modeling strategy. *Annu. Rev. Fluid Mech.* **2008**, *40*, 47.
- (28) Zhu, H. P.; Zhou, Z. Y.; Yang, R. Y.; Yu, A. B. Discrete particle simulation of particulate systems: A review of mayor applications and findings. *Chem. Eng. Sci.* **2008**, *63*, 5728.
- (29) Kuang, S. B.; Chu, K. W.; Yu, A. B.; Zou, Z. S.; Feng, Y. Q. Computational investigation of horizontal slug flow in pneumatic conveying. *Ind. Eng. Chem. Res.* **2008**, *47*, 470.
- (30) Li, J.; Mason, D. J. A computational investigation of transient heat transfer in pneumatic transport of granular particles. *Powder Technol.* **2000**, *112*, 273.
- (31) Lim, E. W. C.; Wang, C. H. Diffusion modeling of bulk granular attrition. *Ind. Eng. Chem. Res.* **2006**, *45*, 2077.
- (32) Han, T.; Levy, A.; Kalman, H. Dem simulation for attrition of salt during dilute-phase pneumatic conveying. *Powder Technol.* **2003**, *129*, 92.
- (33) Watano, S. Mechanism and control of electrification in pneumatic conveying of powders. *Chem. Eng. Sci.* **2006**, *61*, 2271.
- (34) Lim, E. W. C.; Zhang, Y.; Wang, C. H. Effects of an electrostatic field in pneumatic conveying of granular materials through inclined and vertical pipes. *Chem. Eng. Sci.* **2006**, *61*, 7889.
- (35) Watano, S.; Saito, S.; Suzuki, T. Numerical simulation of electrostatic charge in powder pneumatic conveying process. *Powder Technol.* **2003**, *135*, 112.
- (36) Kuang, S. B.; Yu, A. B.; Zou, Z. S. A new point-locating algorithm under three-dimensional hybrid meshes. *Int. J. Multiphase Flow* **2008**, *34*, 1023.
- (37) Chu, K. W.; Yu, A. B. Numerical simulation of the gas-solid flow in three-dimensional pneumatic conveying bends. *Ind. Eng. Chem. Res.* **2008**, *47*, 7058.
- (38) Lim, E. W. C.; Wang, C. H.; Yu, A. B. Discrete element simulation for pneumatic conveying of granular material. *AIChE J.* **2006**, *52*, 496.
- (39) Fraige, F. Y.; Langston, P. A. Horizontal pneumatic conveying: A 3d distinct element model. *Granular Matter* **2006**, *8*, 67.

- (40) Strauss, M.; McNamara, S.; Herrmann, H. J.; Niederreiter, G.; Sommer, K. Plug conveying in a vertical tub. *Powder Technol.* **2006**, *162*, 16.
- (41) Vasquez, N.; Sanchez, L.; Klinzing, G. E.; Dhodapkar, S. Friction measurement in dense phase plug flow analysis. *Powder Technol.* **2003**, *137*, 167.
- (42) Konrad, K.; Totah, T. S. Vertical pneumatic conveying of particle plugs. *Can. J. Chem. Eng.* **1989**, *67*, 245.
- (43) Krull, T.; Jones, M. G.; Keys, S. Stress-field modeling and pressure drop prediction for slug-flow pneumatic conveying in an aerated radial stress chamber. *Particulate Sci. Technol.* **2004**, *22*, 129.
- (44) Di Felice, R. The voidage function for fluid particle interaction systems. *Int. J. Multiphase Flow* **1994**, *20*, 153.
- (45) Zhou, Y. C.; Wright, B. D.; Yang, R. Y.; Xu, B. H.; Yu, A. B. Rolling friction in the dynamic simulation of sandpile formation. *Phys. A* **1999**, *269*, 536.
- (46) Feng, Y. Q.; Yu, A. B. Microdynamic modelling and analysis of the mixing and segregation of binary mixtures of particles in gas fluidization. *Chem. Eng. Sci.* **2007**, *62*, 256.
- (47) Feng, Y. Q.; Xu, B. H.; Zhang, S. J.; Yu, A. B.; Zulli, P. Discrete particle simulation of gas fluidization of particle mixtures. *AIChE J.* **2004**, *50*, 1713.
- (48) Launder, B. E.; Spalding, D. B. The numerical computation of turbulent flows. *Comput. Methods Appl. Mech. Eng.* **1974**, *3*, 269.
- (49) Lain, S.; Grillo, C. A. Comparison of turbulent particle dispersion models in turbulent shear flows. *Braz. J. Chem. Eng.* **2007**, *24*, 351.
- (50) Crowe, C. T. On models for turbulence modulation in fluid-particle flows. *Int. J. Multiphase Flow* **2000**, *26*, 719.
- (51) Lightstone, M. F.; Hodgson, S. M. Turbulence modulation in gas-particle flows: A comparison of selected models. *Can. J. Chem. Eng.* **2004**, *82*, 209.
- (52) Cundall, P. A.; Strack, O. D. L. Discrete numerical-model for granular assemblies. *Geotechnique* **1979**, *29*, 47.
- (53) Partankar, S. V. *Numerical Heat Transfer and Fluid Flow*; Hemisphere Publishing Co.: Washington, DC, 1980.
- (54) Ferziger, J.; Peric, M. *Computational Methods for Fluid Dynamics*, 3rd ed; Springer: New York, 2002.
- (55) Henty, D. S. Performance of hybrid message-passing and shared-memory parallelism for discrete element modeling. Proceedings of the SC 2000 Conference, Dallas, TX, 2000.
- (56) Konrad, K.; Davidson, J. F. The gas-liquid analogy in horizontal dense-phase pneumatic conveying. *Powder Technol.* **1984**, *39*, 191.
- (57) Pan, R.; Wypych, P. W. Pressure drop and slug velocity in low-velocity pneumatic conveying of bulk solid. *Powder Technol.* **1997**, *94*, 123.
- (58) Mi, B.; Wypch, P. W. Pressure-drop prediction in low-velocity pneumatic conveying. *Powder Technol.* **1994**, *81*, 125.
- (59) Borzone, L. A.; Klinzing, G. E. Dense-phase transport-vertical plug flow. *Powder Technol.* **1987**, *53*, 273.
- (60) Li, J.; Pandiella, S. S.; Webb, C.; McGlinchey, D.; Cowell, A.; Xiang, J.; Knight, L.; Pugh, J. An experimental technique for the analysis of slug flows in pneumatic pipelines using pressure measurements. *Particulate Sci. Technol.* **2002**, *20*, 283.
- (61) Kawaguchi, T.; Tanaka, T.; Tsuji, Y. Numerical analysis of density wave in dense gas-solid flows in a vertical pipe. *Prog. Theor. Phys. Suppl.* **2000**, *696*.
- (62) Ratnayake, C.; Datta, B. K.; Melaaen, M. C. A unified scaling-up technique for pneumatic conveying systems. *Particulate Sci. Technol.* **2007**, *25*, 289.
- (63) Niederreiter, G.; Sommer, K. Modeling and experimental validation of pressure drop for pneumatic plug conveying. *Granular Matter* **2004**, *6*, 179.
- (64) Yang, W. C. Correlation for solid friction factor in vertical pneumatic conveying lines. *AIChE J.* **1978**, *24*, 548.

Received for review February 11, 2009
 Revised manuscript received April 16, 2009
 Accepted May 5, 2009

IE900230S